Simultaneous analysis of current–voltage and capacitance–voltage characteristics of metal–insulator–semiconductor diodes with a high mid-gap trap density

P. Cova and A. Singh
Departamento de Física, Universidad de Oriente, Laboratorio de Simulación de Dispositivos Semiconductores, Apartado 124, Cumaná 6101, Sucre, Venezuela

R. A. Masut[a)]
Département de Génie Physique, Groupe de Recherche en Physique et Technologie des Couches Minces, École Polytechnique, C.P. 6079, Succ. Centre-ville Montréal, Québec H3C 3A7, Canada

(Received 17 November 1997; accepted for publication 13 January 1999)

We present an improved method to analyze simultaneously the current–voltage and capacitance–voltage characteristics of metal–insulator–semiconductor (MIS) diodes. We use the method to study the effect of Zn doping concentration on the current transport in Au MIS contacts fabricated on $In_{0.21}Ga_{0.79}As$ layers grown by metalorganic vapor phase epitaxy on highly doped GaAs substrates. At room temperature and for low reverse bias voltage, the generation/recombination process via mid-gap traps is the only dominant mechanism in these MIS diodes. For high reverse bias, both this mechanism and thermionic-field emission control current transport. The generation/recombination current observed is due to donor type mid-gap traps whose density shows an almost linear dependence with Zn concentration. The value of the barrier height at zero bias and at room temperature ($\phi_{b0}=0.73\ \mathrm{V}\pm 12\%$) is independent of the Zn concentration. For the procedure used to prepare the $In_{0.21}Ga_{0.79}As$:Zn surfaces, the thickness of the oxide layer and the transmission coefficient of holes across this layer depend on the Zn doping concentration in the range $7\times10^{14}\leqslant N_A\leqslant 5\times10^{18}\ \mathrm{cm}^{-3}$. Zn doping seems to inhibit the formation of the unintentional native oxide on the surface of $In_{0.21}Ga_{0.79}As$ epilayers. © *1999 American Institute of Physics.*
[S0021-8979(99)02508-6]

I. INTRODUCTION

Damages in the form of defects, such as vacancies, interstitials, complex impurity clusters, and dislocations, introduce deep levels in the band gap of semiconductors which are associated with many undesirable aspects of the performance and reliability of devices. A simple way to study mid-gap traps is the analysis of current–voltage ($I-V$) characteristics in a Schottky diode taking into account the recombination–generation (RG) process that they induce. Many models have been used to analyze the forward and reverse $I-V$ data of MIS diodes.[1–7] However, few papers have analyzed $I-V$ characteristics simultaneously with capacitance–voltage ($C-V$) data to obtain the diode characteristic parameters.[3–5] This simultaneous analysis of the $I-V$ and $C-V$ data avoids the conflicting results often found in the literature where the Schottky barrier height values obtained from different measurement techniques ($I-V$, $C-V$, internal photoemission, etc.) are generally different.[1,2] In a previous article, we have developed an approach to simultaneously analyze $I-V$ and $C-V$ characteristics in a MIS diode. This approach considers the bias dependence of interface states distribution and the barrier lowering due to the image force.[3,4] It is applicable when the interfacial-layer thermionic emission (ITE) and the interfacial-layer diffusion (ID) mechanisms compete to limit current transport. The formalism works remarkably well for MIS contacts fabricated on an epitaxial layer with a low trap density.[3,4] For an epilayer with a high trap density, however, this formalism cannot explain the $I-V$ data since the ITE and ID mechanisms will no longer be dominant.

Recently, we have also developed an approach to simultaneously analyze $I-V$ and $C-V$ characteristics in a Schottky diode also taking into account the RG process.[5] As with different formalisms proposed in the literature for the RG current, that approach was based on the depletion approximation which does not hold for devices with a high mid-gap trap density. In this article we propose an improved method to analyze simultaneously the reverse $I-V$ and high frequency $C-V$ data of an MIS diode with a high mid-gap trap density. Based on the numerical solution of the nonlinear Poisson's and continuity equations, this approach no longer uses the depletion layer approximation or the Mott–Schottky equation to fit the $C-V$ data. We use this method to revise the study of current transport in Au Schottky contacts to epitaxial $In_{0.21}Ga_{0.79}As$:Zn layers presented in Ref. 1 and to determine the Zn doping dependence of the mid-gap traps in these diodes. The present study differs from that of Ref. 1 in two aspects: first, we analyze *simultaneously* the reverse $I-V$ and high frequency $C-V$ data and not the forward $I-V$ and high frequency $C-V$ data, independently, as was done in Ref. 1; and second, we present a study of the Zn doping dependence of the mid-gap traps (in contrast with surface

a)Electronic mail: masut@email.phys.polymtl.ca

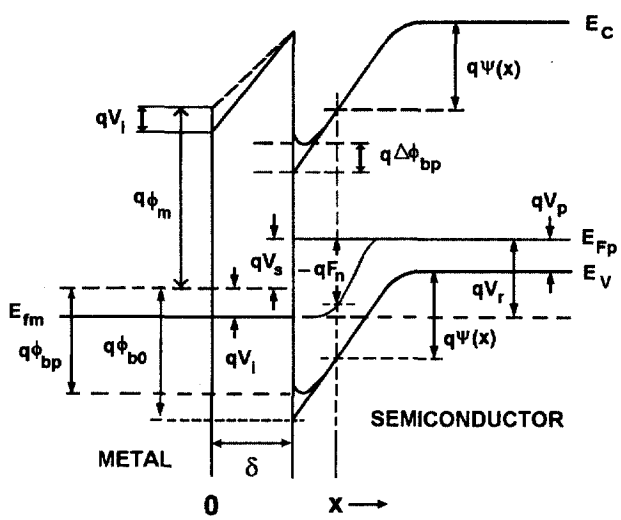

FIG. 1. Energy-band diagram of a metal/p-type semiconductor Schottky diode with a thin interfacial layer for a reverse applied bias.

states) in thick epitaxial layers of $In_{0.21}Ga_{0.79}As$:Zn. Other important findings in this article are: (i) the functional relation between Zn doping and the density of mid-gap traps introduced in $In_{0.21}Ga_{0.79}As$ epilayers and (ii) the indirect experimental evidence that Zn doping inhibits unintentional oxidation of the $In_{0.21}Ga_{0.79}As$ surface.

II. THEORETICAL BACKGROUND

A. Reverse I–V characteristics of an MIS diode with a high density of mid-gap traps

The energy-band diagram for an MIS contact, with an applied reverse bias V_r, fabricated on a p-type semiconductor is shown in Fig. 1, where δ is the insulator layer thickness, ϕ_m is the work function of the metal, and $\Delta\phi_{bp}$ is the image force lowering and is given by

$$\Delta\phi_{bp}=[q^3N_A(\phi_{b0}+V_s-V_p)/8\pi^2\epsilon_s^3]^{1/4}. \tag{1}$$

In this equation, N_A is the shallow acceptor concentration, ϕ_{b0} is the barrier height at zero bias, ϵ_s is the semiconductor permittivity, and qV_p is the energy difference between the majority carrier Fermi level E_{fp} and the top of the valence band edge in the bulk E_V. V_s is the applied voltage drop across the surface depletion layer of the semiconductor and is related to the applied voltage V_r through the equation $V_s=V_r-V_i$, where V_i is the applied voltage drop across the interfacial layer and is measured with respect to its value at zero bias.

In Fig. 1, $\psi(x)$ is the electrostatic potential at distance x from the interface, which is taken as zero in the back ohmic contact ($x=L$) and is measured with respect to the top of the valence band $\{q\psi(x)=-[E_V(x)-E_V(L)]\}$. L is the thickness of the $In_{0.21}Ga_{0.79}As$ epitaxial layer and E_{fn} is the electron quasi Fermi level. In this work, F_n represents the electron quasi Fermi level expressed in volts and measured with respect to its value in the back ohmic contact $\{F_n(x)=[E_{fn}(x)-E_{fn}(L)]/q\}$ and ϕ_{bp} is the barrier height at the reverse bias V_r given by

$$q\phi_{bp}=q\phi_{b0}-q\Delta\phi_{bp}. \tag{2}$$

The importance of the contribution of the RG current I_{RG} to the total current of a Schottky diode was convincingly demonstrated in a classic paper by Yu and Snow[8] and for a reverse applied bias it is expressed as

$$I_{RG}=-qA\int_{\delta+x_{min}}^{\delta+L}R\,dx \tag{3}$$

with

$$R=N_tC_pC_n\frac{[p(x)n(x)-n_i^2]}{C_pp(x)+e_p+e_n}, \tag{4}$$

where R is the recombination–generation rate, A is the area of the Schottky contacts (4.76×10^{-4} cm^2), $C_p(=\sigma_p v_{p,th})$ and $C_n(=\sigma_n v_{n,th})$ are the hole and electron capture coefficients, σ_p and σ_n are the capture cross sections for holes and electrons, and $v_{p,th}(v_{n,th})$ are the hole (electron) thermal velocities. $e_p(=C_pn_i/\gamma)$ and $e_n(=\gamma C_nn_i)$ are the hole and electron emission rates and γ is the statistical weight factor for deep impurities.[9] The minus sign on the right hand side of Eq. (3) arises since R is negative for a reverse bias and the majority-carrier current is considered positive when the hole moves to the right at the interface (Fig. 1). In Eq. (3), x_{min} is the location of the band minimum due to image force lowering, N_t is the trap density, n_i is the intrinsic carrier density, and n and p are the electron and hole densities, which are defined by

$$p(x)=p_0\exp[-\beta\psi(x)]$$

and

$$n(x)=\frac{n_i^2}{p_0}\exp\{\beta[\psi(x)+F_n(x)]\}, \tag{5}$$

where $\beta=q/kT$ and p_0 is the hole density at the ohmic back contact.

The RG process normally takes place via localized states, and according to the Schockley–Read theory,[10,11] the most effective centers are those with energies lying near the center of the forbidden gap. Therefore, in Eq. (4), the energy level of the recombination centers E_t is considered equal to the intrinsic level E_i and $n\ll p$ for a p-type semiconductor. It has been experimentally shown[3–5] that for an MIS contact fabricated on an epitaxial layer, the contribution of ID to the total current is negligible in comparison with other mechanisms. Therefore, the interfacial-layer diffusion mechanism is ignored in this work. Furthermore, the Fermi level for the majority carriers (E_{fp}) will be assumed constant across the space-charge layer of the semiconductor.[9]

At room temperature, holes can virtually have enough energy to pass below the bottom of the valence band, and they can be emitted into the metal by traversing the insulator layer. This is known as ITE and the expression for the current $I_{r,ITE}$ is given in Ref. 4. Under certain circumstances it may also be possible for holes with an energy E_m above the bottom of the valence band to penetrate the barrier by quantum-mechanical tunneling. This is known as thermionic-field emission TFE.[12,13] The tunneling through the barrier becomes significant at lower doping levels in reverse bias;

more than under forward bias because the reverse bias voltages involved are usually much greater. Furthermore, the application of only a moderately large reverse bias can cause the potential barrier to become thin enough for significant tunneling of holes from the metal to the semiconductor to take place even at low doping levels. Tunneling is one of the most common causes of "soft" reverse characteristics. It is particularly important near the MIS interface because the crowding of the field lines causes an increase in the field strength. This decreases the barrier width and exaggerates the image–force lowering ($q\Delta\phi_{bp}$).[4] The effect is accentuated if the surface of the semiconductor next to the insulator is in accumulation (i.e., the hole density is increased) due to the presence of negative surface charges, since this makes the barrier at the interface even thinner.[9] In the thermionic-field regimen, the reverse $I-V$ relationship has been derived by Padovani and Stratton[13] as

$$I_{r,\mathrm{TFE}}=I_s\exp(-V_r/E_0)\exp(\beta V_r) \tag{6}$$

with

$$E_0=E_{00}\coth(\beta E_{00})$$

and

$$E_{00}=\frac{\hbar}{2}\sqrt{\frac{N_{\mathrm{eff}}}{m_p^*\epsilon_s}}, \tag{7}$$

where m_p^* is the hole effective mass, N_{eff} is the effective concentration of holes at the surface of the semiconductor next to the insulator, and I_s is a function of temperature, the barrier height, and other semiconductor parameters. I_s is given approximately by

$$I_s=AA^*\theta_p\frac{T}{k}\sqrt{\pi qE_{00}}\sqrt{q(V_r-V_p)+\frac{q\phi_{\mathrm{eff}}}{\cosh^2(\beta E_{00})}}\times e^{-(\phi_{\mathrm{eff}}/E_0)}, \tag{8}$$

where A^* is the Richardson constant, given by $A^*=1.2\times10^6(m_p^*/m_0)\mathrm{A\,m^{-2}\,K^{-2}}$.[9,12] θ_p is the transmission coefficient of holes across the interfacial layer and $q\phi_{\mathrm{eff}}(=q\phi_{b0}-q\Delta\phi_{bp}-\alpha V_r)$ is the effective barrier height at reverse bias V_r and temperature T.[1,12] The last term in the expression of $q\phi_{\mathrm{eff}}$ is related to the effect of the insulator layer on the $I-V$ characteristics. The reduction of current due to tunneling through the insulator layer is also a departure from ideal behavior described frequently by an ideality factor (n value) which increases with increasing insulator thickness. α can be approximated by[12]

$$\alpha=\frac{1}{1+\dfrac{Aq^2N_{\mathrm{ss}}}{C_{\mathrm{SC}}}+\dfrac{C_i}{C_{\mathrm{SC}}}}, \tag{9}$$

where N_{ss} is the energy density of the interface states expressed in $\mathrm{eV^{-1}\,cm^{-2}}$, C_i is the capacitance of the insulator layer ($=A\epsilon_i/\delta$),[4,5] ϵ_i represents the insulator permittivity, and C_{SC} is the semiconductor depletion-layer capacitance. For all MIS diodes analyzed in this work, the value of $Aq^2N_{\mathrm{ss}}/C_{\mathrm{SC}}$ was small at reverse bias, i.e., $Aq^2N_{\mathrm{ss}}/C_{\mathrm{SC}}\ll C_i/C_{\mathrm{SC}}$ [to verify this inequality the N_{ss} values were obtained from Ref. 1], then α can be expressed as $\alpha=(1+C_i/C_{\mathrm{SC}})^{-1}$ and is thus independent of N_{ss}.

The ITE and TFE are two emission processes effectively in parallel. Therefore, for a value V_r of reverse voltage, the majority-carrier current at the interface is given by

$$I_{r,p}(\delta+x_{\min})=I_{r,\mathrm{ITE}}+I_{r,\mathrm{TFE}} \tag{10}$$

and the reverse electric current can be written as:[4,5]

$$I_r=I_{\mathrm{th}}[1-e^{-\beta V_r}]+I_se^{-V_r/E_0}e^{\beta V_r}+I_{\mathrm{RG}}, \tag{11}$$

where $I_{\mathrm{th}}=AA^*T^2\theta_p\exp[-\beta(\phi_{bp}-V_i)]$.

The electrostatic potential $\psi(x)$ as a function of distance can be obtained solving the one-dimensional Poisson's equation, which is defined by

$$\epsilon_s\,d^2\psi(x)/dx^2=-\rho(x)$$

with

$$\rho(x)=q[p-N_A+N_t^*], \tag{12}$$

where ϵ_s is the semiconductor static dielectric constant, and N_t^* is the concentration of ionized deep impurities with an appropriate sign and statistical weight factor depending on the trap type.

The quasi Fermi level for electrons and F_n as functions of distance can be obtained by using the one-dimensional continuity equation for electrons, which is expressed as $dJ_n/dx-qR=0$ for the electron current density J_n. Using Boltzmann's equation and Eq. (5), J_n can be written as $J_n=q\mu_nndF_n/dx$, with μ_n the electron mobility, assumed to be isotropic. By substituting this equation into the electron continuity equation, the dc component of the electron-transport equation can be expressed as:

$$\frac{d}{dx}\left(a(x)\frac{d}{dx}(e^{\beta F_n(x)})\right)-qR=0, \tag{13}$$

where $a(x)$ is given by

$$a(x)=kT\mu_n\frac{n_i^2}{p_0}e^{\beta\psi(x)}. \tag{14}$$

B. Boundary conditions for the differential equations and numerical solution

Special attention is required for the boundary conditions at both edges of the epitaxial layer. Two boundary conditions are required at each edge to solve Eqs. (12) and (13), one for the electrostatic potential $\psi(x)$ and another for $F_n(x)$. If the total device length L is sufficient to assume that both Fermi levels coincide at the ohmic contact edge of the epitaxial layer ($x=L$), we have

$$\psi(\delta+x_{\min})=(V_{\mathrm{bi}}-\Delta\phi_{\mathrm{bp}}+V_s),\quad \psi(L)=0,\qquad F_n(\delta+x_{\min})=-V_r \tag{15}$$

and

$$F_n(L)=0 \tag{16}$$

for a reverse voltage V_r. V_{bi} is the built-in potential, which is needed to make the Fermi levels match throughout the epitaxial layer in the absence of external bias. It is assumed

that both Fermi levels are coincident at the ohmic contact edge of the epilayer $[E_{fn}(L)=E_{fp}(L)=0]$ even under external bias. The value of the hole density p_0 at $x=L$ is easily evaluated by requiring local charge neutrality:

$$p_0 \exp[-\beta\psi(L)]-N_A+N_t^*(L)=0. \tag{17}$$

After the appropriate scaling, Eqs. (12) and (13) are discretized according to a variable size mesh. In the discretization of Poisson's equation, Eq. (12), a simple three-point difference scheme, yielding expressions correct to $O(h^2)$, is used. This allows us to describe correctly the spatial variations of the electrostatic potential. In the current-transport equation [Eq. (13)], the large exponential variations of the carrier densities over several factors of 10 impose a solution procedure like that used by Gummel's iteration method[14] as is explained in the Appendix. The discretized equations are then expressed in terms of ψ and F_n. The use of F_n as an independent variable, instead of n, is advantageous because its variation is smoother and it scales better with the second independent variable ψ. The continuity equation (13) with Poisson's equation (12), yield a set of two second-order nonlinear differential equations. This system is linearized in terms of small corrections of the variables to an appropriate initial guess, and iterated until the desired convergence. In the calculation procedure, we have used an efficient algorithm of the iterative Newton's method with an adaptive mesh refinement (AMR) to adequately solve the basic equations. More details of the discretization process and the solution procedure used in this work to solve the basic equations are given in the Appendix.

C. High frequency C–V characteristics of an MIS diode

At high frequencies (i.e., 1 MHz), the experimental results show that both the equivalent parallel capacitance C_{ss} and conductance G_{ss} of interface states tend to zero for an MIS contact.[3–5] The total capacitance C of the MIS structure is a series combination of C_i and C_{SC}.[4] C_{SC} can be derived from the voltage derivative of the charge Q_{SC} considering that for the high frequency $C-V$ measurements the ac voltage variations have an effect on the carrier concentration but not on the deep level occupancy. To calculate the small signal capacitance we assume that the external applied voltage is $V_s+\delta V_s$, so the potential, hole, and charge densities will be $\psi+\delta\psi$, $p+\delta p$, and $\rho+\delta\rho$, respectively. The Poisson's equation may be written as:

$$\epsilon_s d^2\psi/dx^2+\epsilon_s d^2(\delta\psi)/dx^2=-\rho(x)+q\beta p\,\delta\psi, \tag{18}$$

where p is the dc component of the hole concentration, which is given by Eq. (5). By defining $y=-\delta\psi/\delta V_s$ and using Eqs. (12), (15), and (18), we obtain

$$\epsilon_s d^2y/dx^2=q\beta p y(x)$$

with

$$y(\delta+x_{min})=-1 \quad \text{and} \quad y(L)=0. \tag{19}$$

In the above equation, it was assumed that the effect of the small ac signal to $\Delta\phi_{bp}$ is negligible. On the other hand, under static condition, the stored charge (per unit area) in the p-type semiconductor (Q_{SC}) is given by

$$Q_{SC}=-\int_{\delta+x_{min}}^{\delta+L}\rho(x)dx$$

$$=-q\int_{\delta+x_{min}}^{\delta+L}[p(x)-N_A+N_t^*]dx \tag{20}$$

while dynamically

$$C_{SC}=-\frac{\delta Q_{SC}}{\delta V_s}=q\beta\int_{\delta+x_{min}}^{\delta+L}p(x)y(x)dx. \tag{21}$$

III. EXPERIMENTAL DATA AND ANALYSIS

Four $In_{0.21}Ga_{0.79}As$ epitaxial layers (Mo08, Mo09, Mo13, and Mo14) grown on highly doped p-GaAs substrates by metalorganic vapor-phase epitaxy (MOVPE) were used in this work. The MOVPE growths, carried out at the National Research Council of Canada (NRCC), used a horizontal quartz cold-wall reactor with a graphite susceptor.[15] Layers were approximately 3 μm thick and doped with Zn during growth, using diethylzinc,[16] to carrier concentrations between 7×10^{14} and 5×10^{17} cm^{-3}. For the fabrication of MIS diodes we have used photolithography and lift-off techniques to define the mesa etched rectangular Schottky contacts with area 4.76×10^{-4} cm^2. Before the metal lift-off process, the $In_{0.21}Ga_{0.79}As$ epilayers were degreased with trichloethylene, acetone, and propanol for 10 min at 40 °C, and chemically etched with a $HCl:H_2O$ (1:1) solution for 6 min. Subsequently, the ohmic contacts to p-GaAs substrates were made by thermal evaporation of Au/Zn/Au at a pressure of about 1×10^{-6} Torr and annealed for 6 min at 375 °C. During the metal lift-off, the epilayers were chemically etched again with $HCl:H_2O$ (1:1) solution, rinsed in de-ionized water, dried with N_2, and immediately put in the vacuum system. In this way, unintentional oxidation of the surface was reduced although not eliminated. This native oxide layer grown on the $In_{0.21}Ga_{0.79}As$ surface before Au deposition allowed the realization of the metal–insulator–semiconductor contacts. The final definition of the mesa structure was carried out by wet chemical etching of the whole epitaxial layer and part of the substrate. The details of $I-V$ and $C-V$ measurements have been reported in Ref. 1.

The reverse $I-V$ and 1 MHz $C-V$ characteristics of the diodes, measured at room temperature, were analyzed simultaneously using a self-consistent algorithm similar to the one proposed in Ref. 5. The main difference in the method proposed here is that we no longer use the depletion layer approximation. Instead, we numerically solved Poisson's equation and used theoretical expressions (11) and (21) to obtain the current and capacitance, respectively, as a function of applied bias. The best fits (solid curves) of reverse $I-V$ data to Eq. (11) are shown in Fig. 2. It is important to point out that the analysis of the low forward $I-V$ characteristics for the four diodes (see Fig. 3 in Ref. 1) shows that the current due the surface leakage at the mesa edges is negligible in

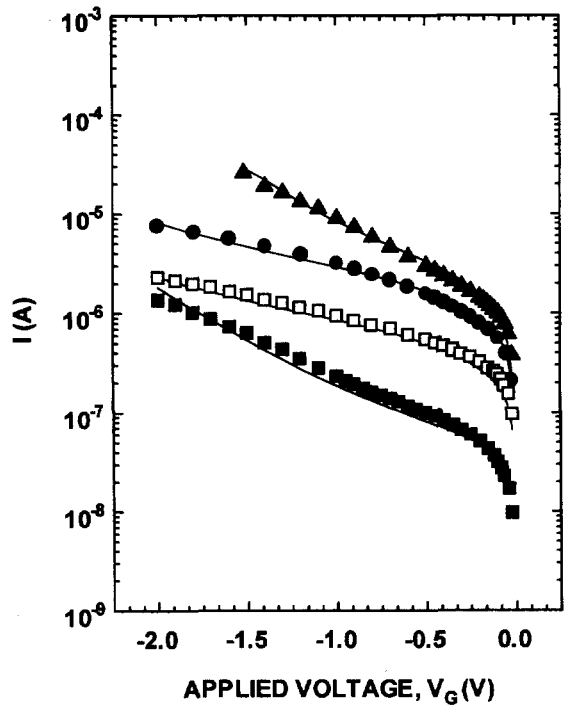

FIG. 2. Room temperature reverse $I-V$ characteristics of the $Au/In_{0.21}Ga_{0.79}As$:Zn epitaxial MIS diodes. The discrete points are the measured values of the majority-carrier current under reverse bias for the four samples; (▲) Mo13, (●) Mo09, (□) Mo14, and (■) Mo08. The solid curves represent the best fits of the experimental data to Eq. (11).

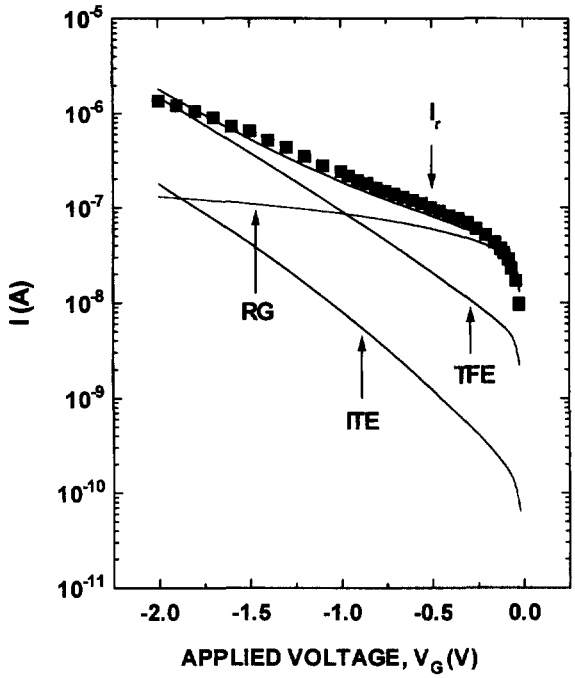

FIG. 4. Contributions of different current–transport mechanisms of an $Au/In_{0.21}Ga_{0.79}As$:Zn epitaxial MIS diode fabricated on the lightly doped sample (Mo08); interfacial-layer thermionic emission (ITE), thermionic-field emission (TFE), and the recombination–generation (RG) process. The discrete points are the measured values of the reverse current and the solid curve is the best fit to the experimental data using Eq. (11).

these devices. Therefore, the contribution of the surface leakage mechanism to the total current is not considered in our model. This hypothesis is corroborated by the fits of reverse $I-V$ data to Eq. (11) shown in Fig. 2. The high frequency capacitance C_M measured under forward and reverse bias were corrected for the effect of series resistance to obtain the junction capacitance C.[4,17] The best fits (solid curves) of $C-V$ data to the equation $C^{-1}=C_{SC}^{-1}+C_i^{-1}$ are shown in Fig. 3. The different current–transport mechanisms on lightly (Mo08) and highly (Mo13) doped samples, are shown in Figs. 4 and 5, respectively. In these figures, the solid curves represent the theoretical total current across the MIS junction and the contribution from different current–transport mechanisms (ITE, TFE and RG). The best values of ϕ_{b0}, N_A, N_t, N_{eff}, C_i, θ_p, σ_p, and σ_n obtained by the fitting procedure are listed in Table I. ϕ_{b0} and N_t are shown in Fig. 6. The doping dependence of the concentration of donor type deep impurities N_t was well described by the relation:

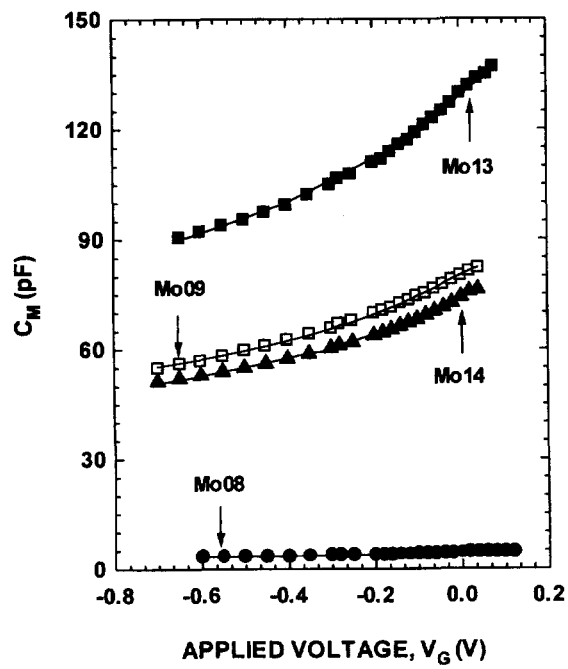

FIG. 3. Room temperature and 1 MHz frequency $C-V$ characteristics under forward and reverse bias of the $Au/In_{0.21}Ga_{0.79}As$ MIS diodes. The discrete points are the measured values and the solid curves are the best fits of the experimental data to equation $C^{-1}=C_{SC}^{-1}+C_i^{-1}$.

$$N_t = 1.1\times 10^{-3}\ N_A^{1.12} \tag{22}$$

with N_t and N_A in cm^{-3}. For Mo13 (the sample with the highest doping concentration), the charge density and generation rate versus distance obtained from the numerical solution of Eqs. (12) and (13) are shown in Fig. 7. Using a value of $\epsilon_i = 7\epsilon_0$[18] for all samples, values of C_i listed in Table I and the relation $C_i = A\epsilon_i/\delta$, we estimate the insulator layer thickness δ grown unintentionally on the four samples. Figure 8 shows the thickness as a function of the Zn doping concentration. We also included in Fig. 8 a point corresponding to an MIS Au/InP:Zn Schottky diode obtained following similar fabrication processes.[4]

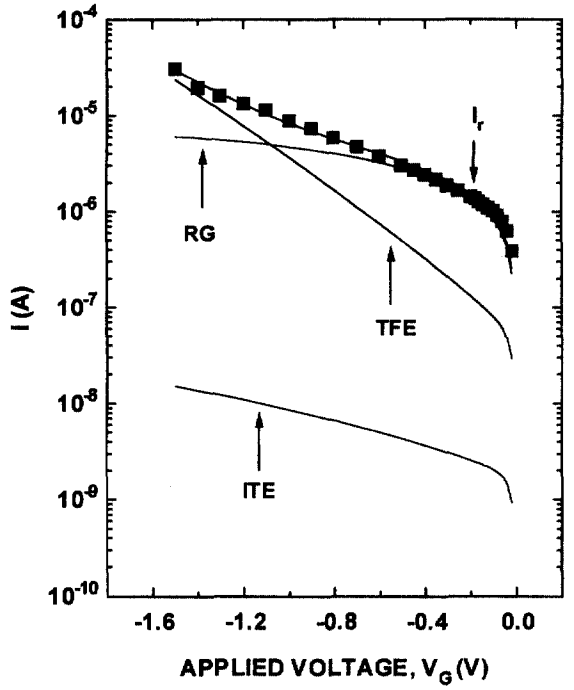

FIG. 5. Contributions of different current–transport mechanisms of an $Au/In_{0.21}Ga_{0.79}As$:Zn epitaxial MIS diode fabricated on the highly doped sample (Mo13); interfacial-layer thermionic emission (ITE), thermionic-field emission (TFE), and the recombination–generation (RG) process. The discrete points are the measured values of the reverse current and the solid curve is the best fit to the experimental data using Eq. (11).

IV. DISCUSSION

Within the reasonable approximations used to simplify and resolve the two fundamental equations of an MIS diode [Eqs. (12) and (13)], two well known and widely accepted approximate treatments are the depletion approximation (DA) and the abrupt charge boundary approximation (ACBA).[9,12,19,20] These approximations simplify the mathematics by taking the trap, electron, and hole densities to be negligible in comparison with the shallow doping density $[\rho(x)=-qN_A]$ in the depletion or space-charge region of the semiconductor $(0\leq x\leq W_{DA})$. Outside this region, the electric potential and charge concentration are those that would exist in the absence of an MIS junction, $\rho(x)=0$. By using DA and ACBA for the case of reverse bias, R and I_{RG} simplify to $R_{DA}=-N_tC_pC_nn_i/(C_p/\gamma+\gamma C_n)$ and $I_{RG.DA}$ $=qARW_{DA}$, where $W_{DA}=[2\epsilon_s(\phi_{b0}+V_s-V_p)/qN_A]^{1/2}$, $V_p=(1/\beta)\mathrm{Ln}(N_V/p_0)$ and N_V is the valence band effective density of states.

TABLE I. The characteristic parameters obtained from the analysis of room temperature $I-V$ and $C-V$ data.[a]

Parameter	Units	Mo08	Mo14	Mo09	Mo13	Estimated % error
ϕ_{b0}	V	0.808	0.719	0.706	0.675	±12
N_A	$10^{17}\,cm^{-3}$	0.0067	1.65	1.89	4.85	±8
N_t	$10^{16}\,cm^{-3}$	0.0052	0.847	2.93	9.04	±13
N_{eff}	$10^{18}\,cm^{-3}$	2.56	1.96	1.96	3.16	±16
C_i	nF	0.033	1.85	3.07	4.73	±12
θ_p		0.0039	0.014	0.028	0.0084	±10

[a]For all samples, $\sigma_p=(0.98\times10^{12}\pm10\%)\,cm^2$ and $\sigma_n=(0.084\times10^{12}\pm10\%)\,cm^2$.

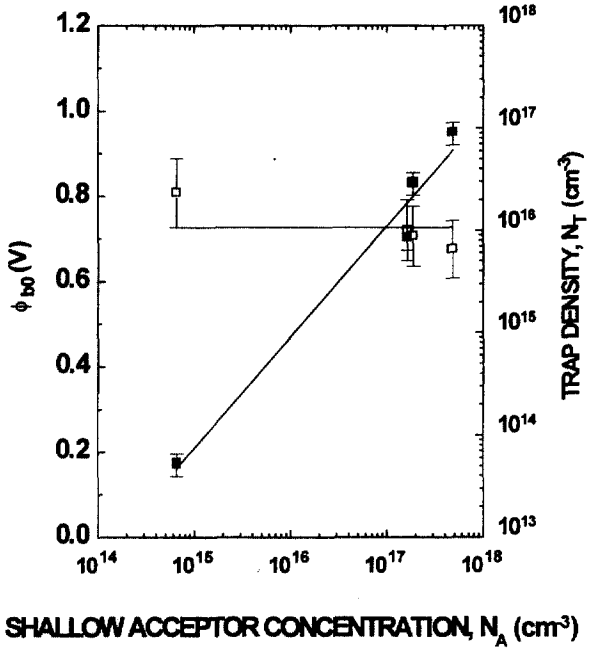

FIG. 6. Zn doping dependence of $\phi_{b0}(\square)$ and $N_t(\blacksquare)$ for $Au/In_{0.21}Ga_{0.79}As$:Zn MIS diodes. The discrete points are the values obtained from the numerical solution. The solid curves are the best fits of the extracted values of ϕ_{b0} and N_t to $\phi_{b0}=0.727\,eV$ and $N_t=1.1\times10^{-3}N_A^{1.12}$, respectively.

The numerical solution obtained from our analysis for the charge density $-\rho/q$ was compared with the DA and

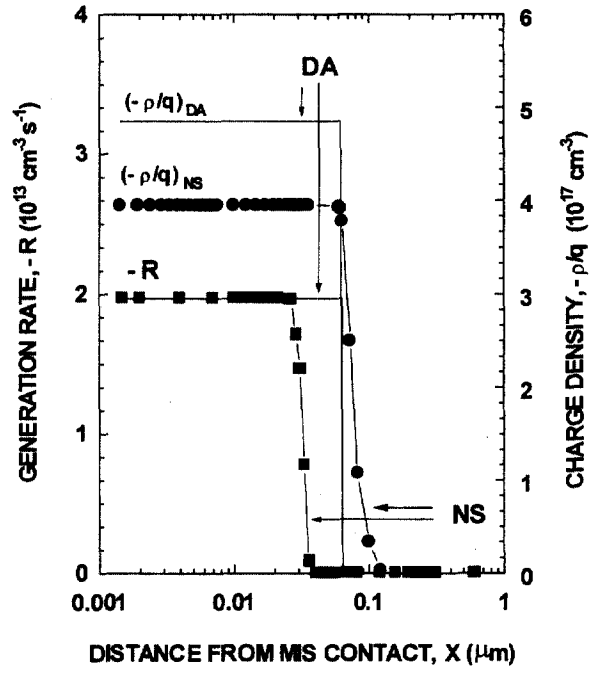

FIG. 7. Charge density and generation rate vs distance for sample Mo13. The discrete points are the values obtained from the numerical solution (NS), and the solid curve, the values calculated from the depletion theory approximation (DA).

ACBA in Fig. 7 (see scale on the right). Our results for the charge density ($3.95\times10^{17}\,cm^{-3}$, see Fig. 7) in the depletion region is clearly less than the shallow acceptor density ($4.85\times10^{17}\,cm^{-3}$). This result is qualitatively the same for the other samples. Therefore, the analysis of $C-V$ data in terms of the Mott–Schottky equation introduces error when MIS diodes have a relatively high trap density ($N_t/N_A>0.05$), since this equation is based on DA and ACBA. The numerical solution obtained for the generation rate R of sample Mo13 was also compared with DA and ACBA in Fig. 7 (see scale on the left). Figure 7 clearly shows where the carrier generation takes place. The limit of the depletion region (as obtained from DA and ACBA) was $W_{DA}=0.069\,\mu m$ for the sample with the highest doping concentration (Mo13,$N_A=4.85\times10^{17}\,cm^{-3}$). However, defining W_{RG} as the value of x for which R (as obtained from our analysis) is half of its maximum value, we find that $W_{RG}=0.033\,\mu m$, which is clearly less than the width in the DA ($W_{DA}=0.069\,\mu m$). Similar results have been previously reported by Schmeits *et al.*[21] On the other hand, for the four samples, the value of I_{RG} obtained from the numerical solution is about half the value calculated from the DA and ACBA. These results suggest that the form of the expression giving R does not allow the derivation of a simple analytical expression for the voltage dependence of I_{RG}.

The experimental values of the majority-carrier current under reverse bias for all samples. (Fig. 2, discrete points) gave a good fit (solid curves) to our theoretical Eq. (11) only for the case of donor-type deep impurities. A careful examination of Figs. 4 and 5 reveals that for low reverse bias, the generation process via mid-gap traps was the dominant mechanism of current transport across the MIS diodes. For higher values of reverse voltage, this mechanism together with thermionic-field emission control current transport. The width of the potential barrier decreases with the increase in reverse voltage, which also increases the tunneling of holes from the metal to the semiconductor. For all samples, the contribution of the interfacial-layer thermionic emission to total current was negligible. This result suggests that at reverse bias and due to the high Schottky barrier of our MIS diodes (Table I), holes do not have enough energy to pass below the bottom of the valence band at x_{min}.

The extracted values of the donor type trap density were well fitted to $N_t=1.1\times10^{-3}N_A^{1.12}$ indicating an almost linear dependence. The increase of N_t with Zn doping suggests that zinc atoms may introduce damage in the $In_{0.21}Ga_{0.79}As$ epitaxial layers as defects or mid-gap levels. A similar result was reported previously by Cova *et al.*[5] and Whitney *et al.*[22] for deep levels observed in InP:Zn (Ref. 5) and $In_{0.53}Ga_{0.47}As/InP$[22–24] epitaxial layers, respectively. The values of ϕ_{b0} extracted by our method (Fig. 6) are independent of Zn doping density within their margins of experimental error, similar to Au/InP:Zn MIS diode.[5] This result suggests that the value of ϕ_{b0} is controlled by the metal and the semiconductor, independent of doping level. The average value of ϕ_{b0} was ($0.73\pm12\%$) V for N_A between 7×10^{14} and $5\times10^{17}\,cm^{-3}$.

From Fig. 8, the values of the insulator layer thickness δ in Å were well fitted to $\delta=2.35\times10^{13}N_A^{-0.76}$ (N_A in cm^{-3}).

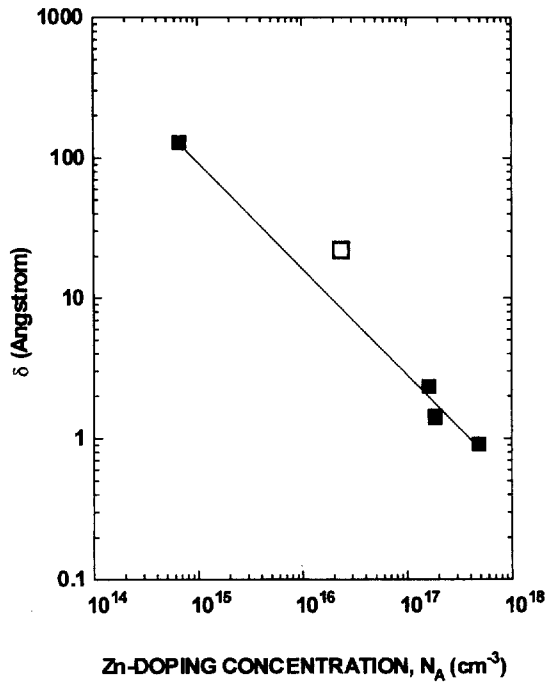

FIG. 8. Zn doping dependence of the oxide layer thickness δ for $Au/In_{0.21}Ga_{0.79}As$ MIS(■) and Au/InP:Zn (□) diodes. The experimental point for a Au/InP:Zn diode was obtained from Ref. 4, those for $Au/In_{0.21}Ga_{0.79}As$ MIS diodes from the numerical solution, and the solid curve is the best fit of the extracted data to $\delta=2.35\times10^{13}N_A^{-0.76}$.

The extracted value of θ_p was also dependent of N_A (see Table I). Thus, for the cleaning procedure used to prepare the $In_{0.21}Ga_{0.79}As$ surface, both the thickness of the oxide layer and the transmission coefficient of holes across this layer depend on Zn doping for concentrations in the range $7\times10^{14}<N_A<5\times10^{17}\,cm^{-3}$. This result is then very important in the analyses of the $I-V$ characteristics of an MIS diode in terms of the well-known and widely used thermionic emission.

The results presented in Fig. 8, which suggest that Zn doping is an inhibitor of the unintentional oxidation of InGaAs surfaces, remain puzzling. It is well known that the oxidation rate of silicon surfaces at high temperatures depends on doping.[25–27] However, as the doping concentration in Si increases, the oxidation rate also increases which is explained by the introduction of more defects aiding the diffusion of oxygen at the interface. In the case of our samples, the density of interface states is higher by 1 order of magnitude in the heavier doped samples (see Ref. 1), which would indicate that more defects are present at the semiconductor–insulator interface. Apparently the nature of these defects is such that they do not promote oxygen diffusion, and thus a higher oxidation rate; they rather inhibit it. Why this happens, however, remains unexplained with the present analysis.

In summary, an improved method for the simultaneous analysis of $I-V$ and $C-V$ data was presented. Using this method a detailed study of the effect of doping concentration on current transport was undertaken in Au MIS contacts on Zn-doped $In_{0.21}Ga_{0.79}As$ layers grown by MOVPE on highly doped GaAs substrates. At room temperature and low re-

verse voltages, independent of the Zn doping concentration, the generation process via mid-gap traps is the only dominant mechanism. For high reverse bias, this mechanism and the thermionic-field emission control current transport. The generation–recombination current in the four diodes studied correlates with the Zn doping density N_A. Zinc atoms introduce damage such as defects in the $In_{0.21}Ga_{0.79}As$ epilayers which act as recombination centers located near the middle of the band gap. The increase in the Zn doping density decreases the effective recombination time in the space-charge region of the semiconductor, and consequently increases the value of I_{RG}. These recombination centers are donor type and their Zn doping dependence is given by $N_t = 1.1 \times 10^{-3} N_A^{1.12}$. The thickness of the oxide layer and the transmission coefficient of holes across this unintentionally grown layer are also dependent on Zn doping. These results suggest that Zn inhibits the formation of the native oxide at the surface of the $In_{0.21}Ga_{0.79}As$ epilayers. The value of $\phi_{b0}(0.73\,V \pm 12\%)$ at room temperature is independent of the Zn doping concentration.

ACKNOWLEDGMENTS

This work was sponsored in part by the Natural Sciences and Engineering Research Council of Canada (NSERC) and the Fonds pour la Formation de Chercheurs et l'Aide à la Recherche (FCAR, Government of Québec).

APPENDIX: NUMERICAL METHOD FOR SOLVING THE BASIC EQUATIONS

This Appendix consist of two subsections; section 1 describes in detail the discretization of the basic equations: Eqs. (12), (13), and (19), and section 2 presents a brief discussion of the numerical procedure used to solve them.

1. Discretization of the basic equations

The method of analysis of $I-V$ and $C-V$ data is based on the solution of the basic nonlinear semiconductor equations: Eqs. (12), (13), and (19). These equations cannot be solved directly and approximate solutions must be considered. One method of approximation is finite differences (simple three-point difference scheme, STPDS) using a nonuniform mesh. This method approximates Eqs. (12), (13), and (19) for the node j on a N mesh with the following equations:

$$\epsilon_s \frac{\dfrac{X_{j+1}-X_j}{h_{j+1}} - \dfrac{X_j - X_{j-1}}{h_j}}{\frac{1}{2}(h_j + h_{j+1})} + \rho_j = 0, \tag{A1}$$

$$\frac{a_{j+\frac{1}{2}} \dfrac{e^{\beta Y_{j+1}} - e^{\beta Y_j}}{h_{j+1}} - a_{j-\frac{1}{2}} \dfrac{e^{\beta Y_j} - e^{\beta Y_{j-1}}}{h_j}}{\frac{1}{2}(h_j + h_{j+1})} - qR_j = 0, \tag{A2}$$

$$\epsilon_s \frac{\dfrac{y_{j+1}-y_j}{h_{j+1}} - \dfrac{y_j - y_{j-1}}{h_j}}{\frac{1}{2}(h_j + h_{j+1})} - q\beta p_j y_j = 0, \tag{A3}$$

where p_j, ρ_j, and R_j are the hole density, charge density, and the recombination–generation rate at node j. X_j and Y_j represent the normalized electrostatic potential and quasi Fermi level, respectively, at the same point, and are given by

$$X_j = \frac{\psi_j}{V_{bi} - \Delta\phi_{bp} + V_s}$$

and

$$Y_j = \frac{(F_n)_j}{V_r}. \tag{A4}$$

In Eq. (A2), $a_{j+1/2}$ and $a_{j-1/2}$ are values of the function $a(x)$ calculated at the mid-points of mesh lines between the node j and the neighboring nodes [Eq. (14)]. Finally, h_j is defined as the length of the mesh line between nodes $j-1$ and j. Since the solutions are accessible only on the nodes, an interpolation scheme is necessary to determine $a_{j\pm 1/2}$. It is common to assume that the electrostatic potential varies linearly between two neighboring nodes. This is equivalent to a constant field along the mesh lines, and the electrostatic potential at the mid-point is obtained by the arithmetic average between two neighboring nodes. Therefore, Eqs. (A1), (A2), and (A3) may be written as:

$$c_1^j X_{j-1} + c_2^j X_j + c_3^j X_{j+1} + c_4^j = 0, \tag{A5}$$

$$c_5^j e^{\beta Y_{j-1}} + c_6^j e^{\beta Y_j} + c_7^j e^{\beta Y_{j+1}} + c_8^j = 0, \tag{A6}$$

$$c_9^j y_{j-1} + c_{10}^j y_j + c_{11}^j y_{j+1} = 0, \tag{A7}$$

where the coefficients c_k^j ($k=1,...,11$ and $j=2,...,N$) are given by

$$c_1^j = \frac{1}{h_j}, \quad c_2^j = -\frac{1}{h_j} - \frac{1}{h_{j+1}}, \quad c_3^j = \frac{1}{h_{j+1}}$$

and

$$c_4^j = \frac{\frac{1}{2}(h_j + h_{j+1})}{\epsilon_s}\rho_j$$

$$c_5^j = \frac{a_{j-\frac{1}{2}}}{h_j}, \quad c_6^j = -\frac{a_{j-\frac{1}{2}}}{h_j} - \frac{a_{j+\frac{1}{2}}}{h_{j+1}}, \quad c_7^j = \frac{a_{j+\frac{1}{2}}}{h_{j+1}} \tag{A8}$$

and

$$c_8^j = \tfrac{1}{2}qR_j(h_j + h_{j+1}),$$

$$c_9^j = \frac{1}{h_j}, \quad c_{10}^j = -\frac{1}{h_j} - \frac{1}{h_{j+1}} - \frac{\frac{1}{2}q\beta p_j(h_j + h_{j+1})}{\epsilon_s}, \tag{A9}$$

and

$$c_{11}^j = \frac{1}{h_{j+1}}. \tag{A10}$$

2. Solution procedure

Since the $(N-1)$ coefficients c_k^j [$k=5,6,...,11$, Eqs. (A9) and (A10)] only depend on the electrostatic potential, the system of equations represented by Eq. (A5) can be solved independently of Eqs. (A6) and (A7) using an iterative method. The values of X_j obtained for a previous voltage are a good initial guess to solve this system of equations

at a given voltage. The electrostatic potential $\psi_j[=(V_{bi}-\Delta\phi_{bp}+V_s)*X_j]$ obtained from the solution of Eq. (A5) is used to update the coefficients c_k^j, solve the systems of Eqs. (A6) and (A7), and thus provide Y_j and y_j values.

In this procedure, we have used an efficient algorithm of the iterative Newton's method to guarantee the convergence of solutions to the systems of equations (A5), (A6), and (A7) from almost any starting point (Globally Convergent Method for Nonlinear Systems of Equations).[28] It is important to point out that to adequately solve these equations a high grid resolution is necessary. For example, solutions to Poisson's equation can exhibit large variations due to local charge concentration near the insulator–semiconductor interface. There are often large portions of the domain where high levels of refinement are not necessary and a highly refined mesh in these regions represents a waste of computational effort. Therefore, we have used the AMR method which allows the concentration of computational efforts where it is necessary, and thus a more accurate solution of the equations. The iteration is started with a coarse mesh of about 50 points. This mesh is gradually refined by halving each interval until the variables do not change in one interval by more than a predetermined quantity, which depends on the desired precision.

[1] A. Singh, P. Cova, and R. A. Masut, J. Appl. Phys. **74**, 6714 (1993).
[2] L. Wang, M. I. Nathan, T-H. Lim, M. A. Khan, and Q. Chen, Appl. Phys. Lett. **68**, 1267 (1995).
[3] P. Cova, A. Singh, and R. A. Masut, Mater. Res. Soc. Symp. Proc. **318**, 507 (1993).
[4] P. Cova, A. Singh, and R. A. Masut, J. Appl. Phys. **82**, 5217 (1997).
[5] P. Cova, A. Singh, A. Medina, and R. A. Masut, Solid-State Electron. **42**, 477 (1998).
[6] P. Cova and A. Singh, Solid-State Electron. **33**, 11 (1990).
[7] D. Donoval, M. Barus, and M. Zodimal, Solid-State Electron. **34**, 1365 (1991).
[8] A. Y. C. Yu and E. H. Snow, J. Appl. Phys. **39**, 3008 (1968).
[9] S. M. Sze, *Physics of Semiconductor Devices* (Wiley, New York, 1981).
[10] W. Schockley and W. T. Read, Jr., Phys. Rev. **87**, 835 (1952).
[11] R. N. Hall, Phys. Rev. **87**, 367 (1952).
[12] D. H. Rhoderick and R. H. Williams, *Metal-Semiconductor Contacts* (Clarendon, Oxford, 1988).
[13] F. A. Padovani and R. Stratton, Solid-State Electron. **9**, 695 (1966).
[14] H. K. Gummel, IEEE Trans. Electron Devices **ED-11**, 455 (1964).
[15] A. P. Roth, M. A. Sacilotti, R. A. Masut, A. Machado, and P. J. D'Arcy, J. Appl. Phys. **60**, 2003 (1986).
[16] R. Benzaquen and A. P. Roth, J. Appl. Phys. **72**, 4288 (1992).
[17] We regret that the reported scale of Fig. 4 in Ref. 1 is not correct. It should read $10^{20}\ F^{-2}$ in place of $10^{18}\ F^{-2}$.
[18] M. Yamaguchi, J. Appl. Phys. **52**, 4885 (1981).
[19] S. J. Pilkington, M. Missous, and D. A. Woolf, J. Appl. Phys. **74**, 6256 (1993).
[20] T. P. Chen, T. C. Lee, C. C. Ling, C. D. Beling, and S. Fung, Solid-State Electron. **36**, 949 (1993).
[21] M. Schmeits, M. Sakhaf, and S. Munnix, J. Appl. Phys. **74**, 6266 (1993).
[22] P. S. Withney and C. G. Fonstad, J. Cryst. Growth **83**, 219 (1987).
[23] S. Forrest and O. Kim, J. Appl. Phys. **53**, 5738 (1982).
[24] M. Ogura, M. Mizuta, K. Onaka, and H. Kukimoto, Jpn. J. Appl. Phys., Part 1 **22**, 1502 (1983).
[25] B. E. Deal and W. Sklar, J. Electrochem. Soc. **112**, 430 (1965).
[26] W. A. Tiller, J. Electrochem. Soc. **128**, 689 (1981).
[27] A. Li, D. A. Antoniadis, and R. W. Dutton, J. Electrochem. Soc. **128**, 1131 (1981).
[28] W. H. Press, W. T. Vetterling, S. A. Teukolsky, and B. P. Flannery, *Numerical Recipes: The Art of Scientific Computing*, 2nd ed. (Cambridge University Press, Cambridge, 1992).